Supporting Information

In situ measurement of thermodynamic partitioning in open hydrogels

Alison Su[†], Benjamin E. Smith[‡], and Amy E. Herr*[†§]

[†]The UC Berkeley/UCSF Graduate Program in Bioengineering, [‡]Department of Vision Sciences, and [§]Department of Bioengineering, University of California Berkeley, Berkeley, California 94720, United States

Table of Contents

Figure S1. Reflection z-series micrographs for correction collar positioning and correction collar position impact on quantitation.

We sought to optimize the position of the correction collar and assess the impact of the collar position on the accuracy of *K* measurements in open microscale hydrogel systems. Inclusion of a correction collar minimizes artefacts arising from a mismatch of *n* between the immersion fluid and coverslip.[1,2] Given that myriad factors alter the effective thickness of a #1.5 coverslip, setting the correction collar at 170 μm for a #1.5 coverslip should not be expected to consistently correct aberrations. Observed deviations from ideal include: a wide tolerance of #1.5 coverslip thicknesses (160 – 190 μm), wear-and-tear of the correction collar over time, and fluctuation in the movable internal lens positions in an objective with temperature.[1] Instead, we adopt a reflection microscopy calibration technique[2] designed to optimize the correction collar setting for each imaging session.

The calibration technique uses reflected laser light to inform adjustment of the correction collar for each specific sample; the reflection is created by an interface with a refractive index mismatch. The intensity of the reflected light at the coverslip/sample interface serves as a proxy for the axial resolution of the microscope and can therefore be used to determine the accurate position of the collar. When the correction collar is accurately positioned, the peak intensity of the reflected light will be maximized. Concomitantly, the full-width half maximum of the axial profile will be minimized. On the other hand, when the correction collar is not positioned accurately, axial aberrations will be present. These axial aberrations will cause a decrease in the measured peak intensity of the reflected light due to the distortion of the excitation light[3] and the axial intensity profile will spread longitudinally.

Using our LSCM system, we imaged the coverslip-sample interface across a range of correction collar positions (140, 150, 170, and 190 μm). As discussed in the main text, we determined the accurate correction collar setting to be 150 μm for #1.5H chambered coverslips (170 ± 5 μm) (**Figure S1A**), a position that differs from the anticipated position by 20 μm.

Having identified the optimal correction collar position for the open microscale hydrogel system, we next sought to understand what impact the position of the correction collar has on fluorescence and *K* quantitation. Testing three different correction collar positions representing under-, accurate, and over-adjustment (140, 150, and 170 μm, respectively), we observed that the position of the correction collar changes the measured solution intensity profile over a given imaging depth (**Figure S1B**). The measured peak fluorescence intensity in-gel and in-solution is lower when the collar is not accurately adjusted, regardless of whether the collar is under- or over-adjusted. Furthermore, we observe different slopes of the solution intensity profile with depth (**Figure S1C**). Interestingly, when the correction collar is over-adjusted (set to 170 μm for #1.5H coverslips), we observe a positive slope of fluorescence with increasing imaging depth. These results for our microscale hydrogel system corroborate previous findings that the position of the correction collar impacts quantitation of measured fluorescence intensity profiles.[2–4] Due to the depth-dependence of fluorescence intensities in both the over- and under-adjusted collar conditions, we anticipated observing a depth-dependent *K*, where $\frac{I_g}{I_{s,c}} \neq \frac{I_g}{I_{s,g}}$. Interestingly, we do not observe a large difference in the *K* measurements at different correction collar positions for 6%T w/v microscale PA hydrogels (**Figure S1D**). We hypothesize that the effect of the correction collar on *K* is mitigated by a combination of a ratiometric measurement and the technical variation introduced by adjusting the correction collar position between every image.

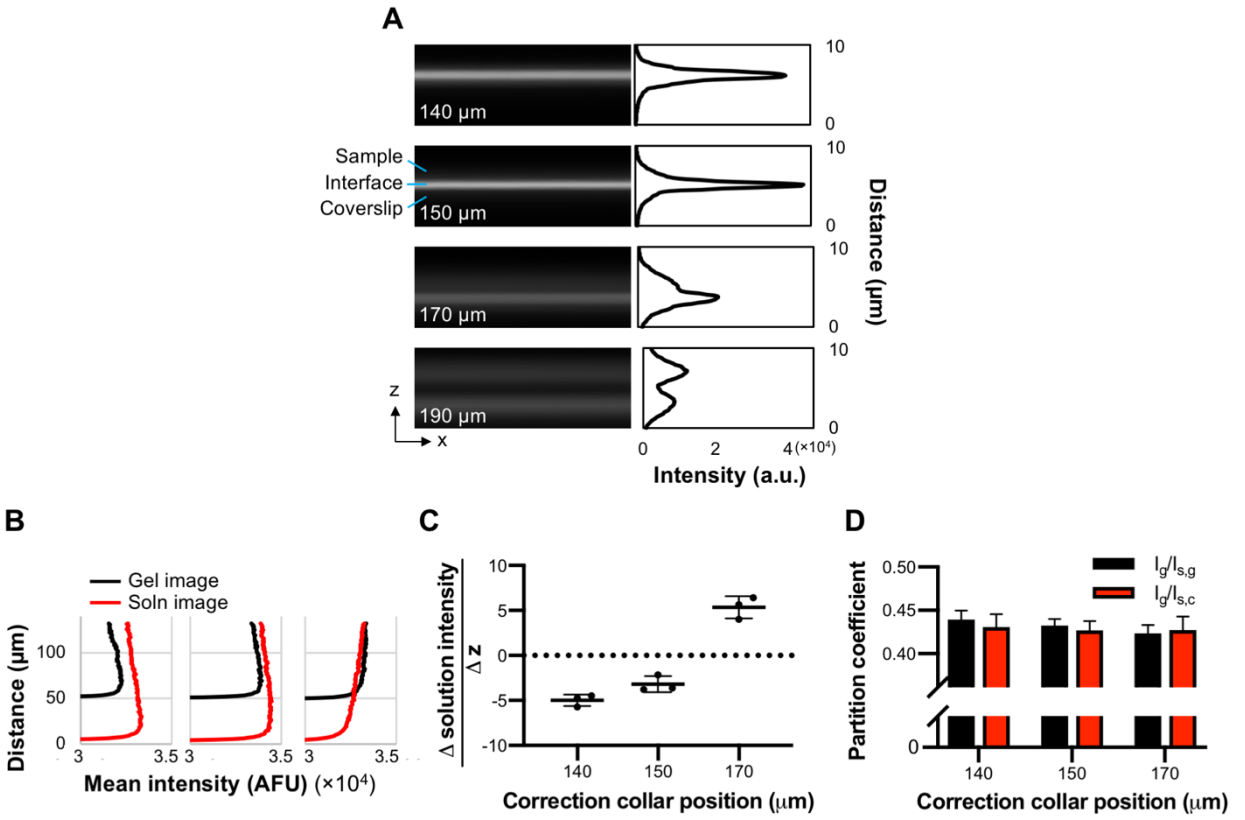

Figure S1. A) Reflection z-series and corresponding intensity profiles of the coverslip-sample interface for accurate correction collar positioning prior to *K* measurements. a.u. = arbitrary units. Numbers in the bottom left of each micrograph indicate the correction collar position. B) Intensity profiles of the solution region from gel and solution images demonstrate the impact of an under-adjusted (140 μm), correctly adjusted (150 μm), and an over-adjusted collar (170 μm), respectively. C) Average slopes of the solution image intensity profiles with increasing depth for different correction collar positions. D) Impact of correction collar positioning on partition coefficient measurements.

Figure S2. Analysis workflow for quantitation.

In line with image processing best practices, the code maintains equal information content (number of optical sections) between micrographs used for the same calculation. A 1 × 1 × 1 3D median filter is applied to the raw micrographs before quantitation to reduce pixel noise while preserving image resolution. To reduce high-frequency noise when identifying the key transition regions, a 1 × 1 × 1 3D Gaussian (low-pass) filter is applied to copies of the micrographs.

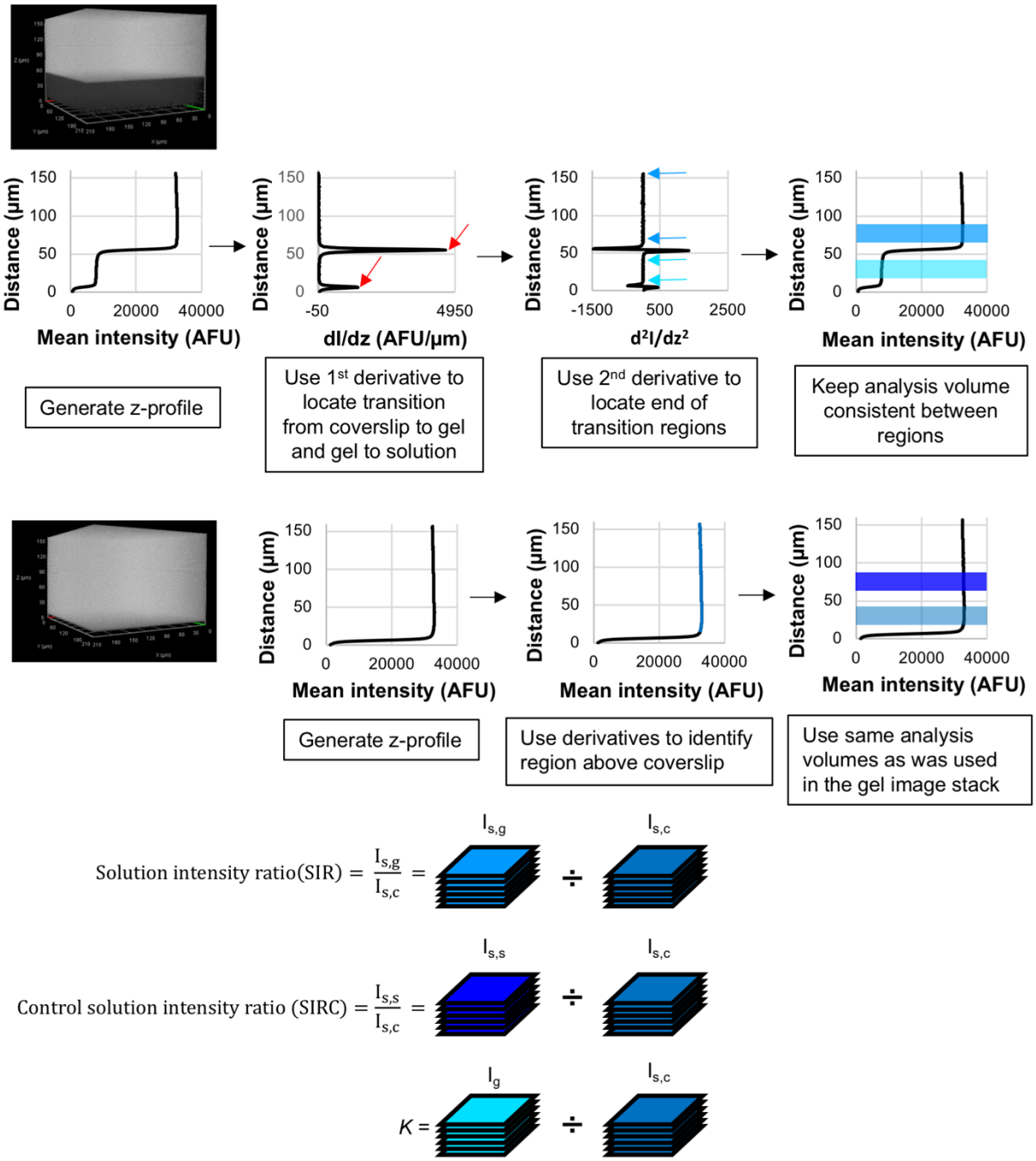

Figure S2. Analysis workflow for automated spatially-resolved *K* calculations and depth-dependent axial aberration quantitation.

Figure S3. Axial optical artefacts caused by refractive index mismatch in the light path.

These data were acquired on a Zeiss LSM 880 NLO AxioExaminer upright microscope using either a 20x/1.0 water immersion objective or a 40x/1.2 water immersion objective equipped with a correction collar. The 633 nm line of a helium-neon laser was used to excite Alexa Fluor 647 and to measure the axial reflection profile of the coverslip-sample interface. Fluorescence was imaged using a 488/561/633 nm dichroic filter and a pinhole set to 0.76 Airy units (20x objective) or 1.3 Airy units (40x objective). Reflected light confocal images were acquired using a T80/R20 partial mirror. Two-dimensional x-z line profiles were captured using the 20x objective as 425.10 μm wide by a z step size of 0.88 μm. Two-dimensional x-z line profiles were captured using the 40x objective as 212.55 μm wide by a z step size of 0.59 μm (fluorescence) or 0.53 μm (reflection).

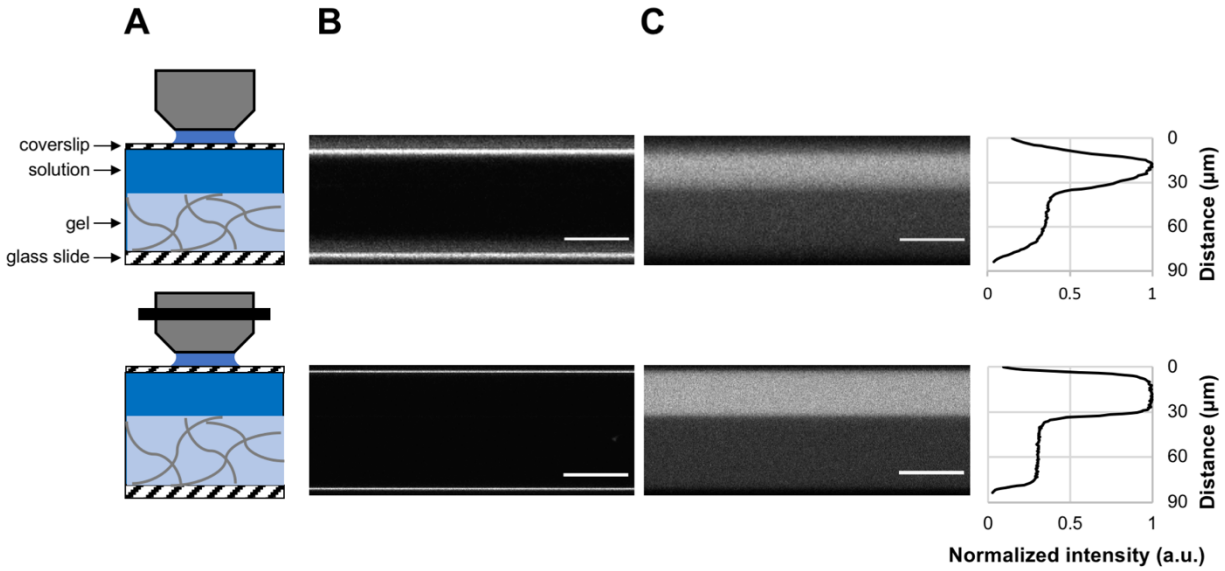

Figure S3. A comparison of micrographs acquired using a water immersion objective (top) and a water immersion objective with a correction collar (bottom). A) Schematic of microscope/sample setup. B) Reflection x-z series from coverslip-solution interface to gel-glass slide interface. C) x-z fluorescence micrographs and normalized intensity profiles of TI* from the same 8%T w/v PA microscale gel. Note that the water immersion objective with correction collar is a 40x/1.2 NA objective, while the water immersion objective is 20x/1.0 NA. Scale bars represent 10 μm in the horizontal direction. The images were cropped to the same field of view. a.u. = arbitrary units.

Figure S4. Image stack division normalizes lateral artefacts.

$$K = \frac{I_g}{I_{s,c}} = \frac{I_{gel}(x,y,z) \times f_{gel}(z) \times f(x,y)}{I_{soln}(x,y,z) \times f_{soln}(z) \times f(x,y)} = \frac{I_{gel} \times f_{gel}(z)}{I_{soln} \times f_{soln}(z)}$$

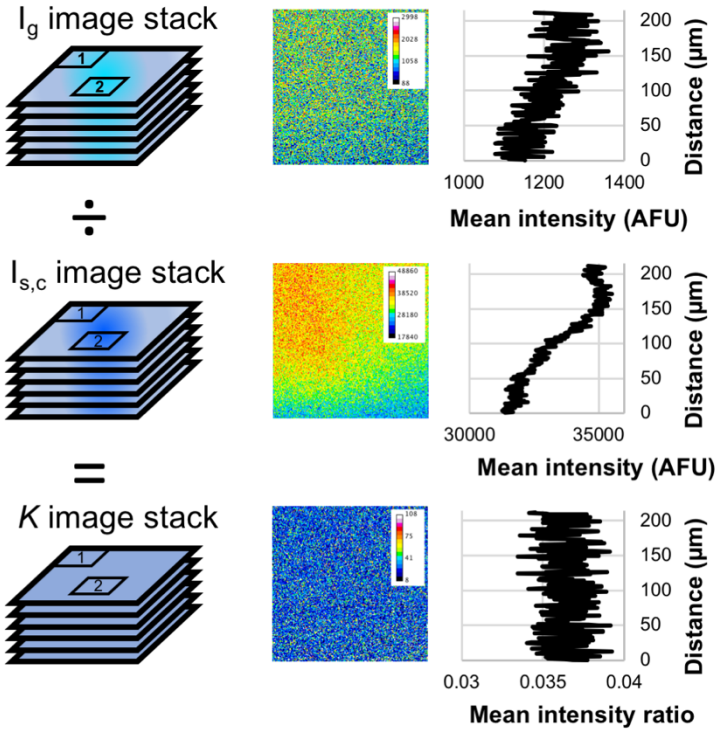

Figure S4. Schematic of the image math performed to calculate *K* (left) and representative micrographs from within the image stacks shown as false-colored heat maps to illustrate lateral artefacts (center) and accompanying intensity profiles (right).

Figure S5. Linear relationship between Ab* concentration and fluorescence intensity.

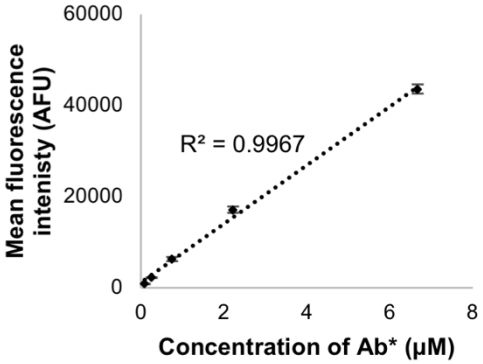

Figure S5. Linear relationship between concentration and mean fluorescence intensity for Alexa-Fluor 647-labeled antibody with a degree of labeling of ~4.3. Analysis was performed on solution at a depth of ~100 μm using a custom macro in ImageJ. Error bars represent standard deviation of triplicate measurements.

Figure S6. Comparison between AC-LSCM and conventional mass-balance technique.

We devised a corollary experiment to compare the AC-LSCM methodology to a conventional mass-balance technique. The solution-depletion mass-balance technique relies on indirect determination of the in-gel solute concentration through measurement of the change in solute concentration in the equilibrating solution.[5–7] To ascertain *K* from the solution-depletion technique, a material balance analysis establishes:

$$K = \frac{V_{sol}}{V_{gel}}\left(\frac{[C]_{0,soln}}{[C]_{f,soln}} - 1\right)$$

Here, V_{sol} and V_{gel} are the volumes of solution and hydrated gel, respectively. $[C]_{0,soln}$ and $[C]_{f,soln}$ are the starting and final concentration of solute in solution, respectively.

Note that practicalities of the mass-balance measurement (i.e., detectable solute fluorescence decrease in bath, mechanical robustness of gels during handling, need to dry surfaces of gels) require gel structures that are notably thicker than those used for AC-LSCM (e.g., 0.04 mm).We fabricated non-attached 6%T PA gels using 2 mm thick spacers, then diced the gels into 9 mm × 19 mm × 2 mm replicates. The surface area of the gels after dicing was estimated using bright-field microscopy. The height of the gels was determined after completion of the experiment. Gels equilibrated with fluorescent solute were sliced in the axial direction to generate thin sections that were gently blotted and placed on their side for imaging the gel height (now in the x-y plane) using widefield fluorescence microscopy. Swollen gels were measured to be ~ 2.2 mm thick and verified using calipers. However, we do note that the accuracy of the mass-balance measurement of *K* relies on the accuracy of the gel thickness measurement, which is subject to some uncertainty. This uncertainty is not present in the AC-LSCM method. The solute studied was TI*. Prior to incubation in TI*, gels were gently blotted with weigh paper to remove excess fluid from the gel surfaces.

Gels were incubated in 400 μl of 1.5 μM TI* for > 24 hours at room temperature in chambered coverslips sealed with Parafilm on a rotator. The ratio of $[C]_{0,soln}$ and $[C]_{f,soln}$ was measured as the ratio of the solution fluorescence in chambers without gel structures (to control for adsorption of solute to the chamber surface) to the solution fluorescence in gel-containing chambers. Fluorescence was measured using a Tecan Infinite M200 Pro with excitation at 640 nm and emission collected at 670 nm. The measured solute-containing solution was re-applied to the gels and the gels were imaged using the AC-LSCM technique adapted for these thicker gels. Given the thickness of the gels required by the solution-depletion technique, SIR or SIR_C (Eq. 5 and 6 of main text) were not directly ascertainable. However, from the measurements of microscale 6%T gels, we know that the solute distribution is uniform and minimal aberrations are induced within a 40-μm imaging depth (Figure 2B of main text). We therefore analyzed < 40 μm into the gel to obtain the AC-LSCM measurements reported in Figure S6 below. Note that because these macroscale gels were not attached to the chambered coverslips, a small fluid layer was present between the coverslip and gel during imaging. The AC-LSCM analysis code was modified for this experiment to account for this new feature. We observe no significant difference between *K* measured using the conventional mass-balance/solution-depletion method and the AC-LSCM technique (Figure S6, N = 3 replicates; $p > 0.9999$, Mann-Whitney U-test). However, we note that the *K* values for TI* measured in the 6%T PA macroscale gels are higher than those measured in the microscale PA gels of the same density, which was unexpected. We hypothesize that this could be due to differences in fabrication setup and potentially different polymerization kinetics between the microscale and macroscale PA gels.

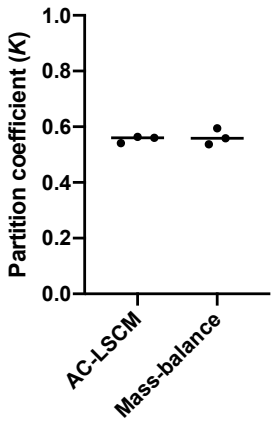

Figure S6. Partition coefficients measured in macroscale gels using the AC-LSCM technique vs. conventional mass-balance/solution-depletion technique are not significantly different (N = 3 replicates, $p > 0.05$, Mann-Whitney U-test).

Figure S7. Relationship between gel height and SIR over varying microscale PA gel densities.

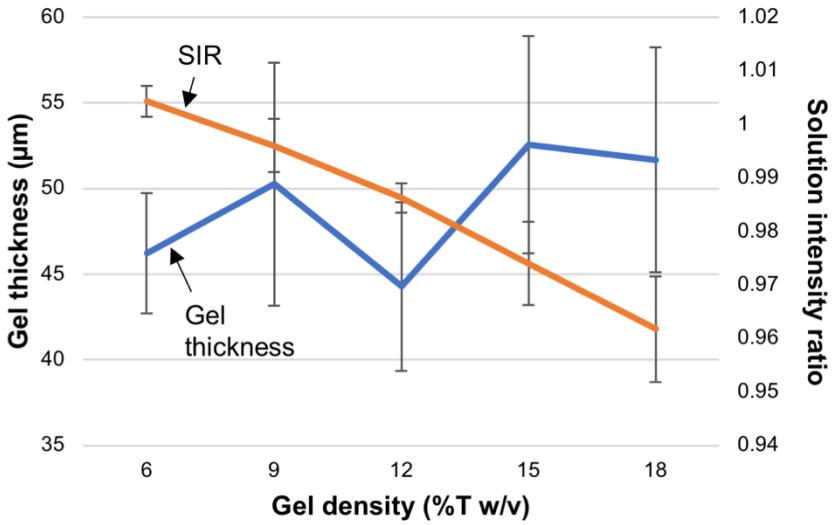

Figure S7. The decrease in solution intensity ratio (SIR) observed with increasing gel density is not caused by increasing gel thickness. Error bars indicate standard deviation for N = 4 replicates.

Figure S8. Impact of over-adjusted correction collar on measured axial artefacts

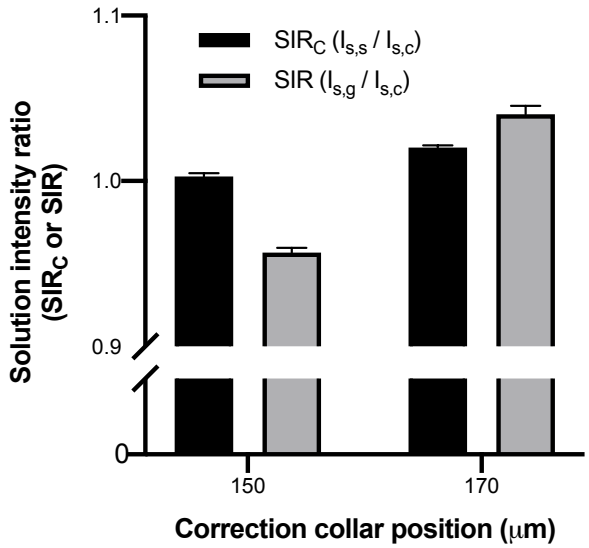

Figure S8. Characterization of axial artefacts in 18%T microscale PA gels when the correction collar is set using reflected light confocal microscopy (150 μm) vs. when the correction collar is set using coverslip thickness specifications (170 μm ± 5 μm). N = 3 replicates.

Figure S9. CV vs. measured aberration (δ_{SIR}) for open microscale PA gels of varying densities.

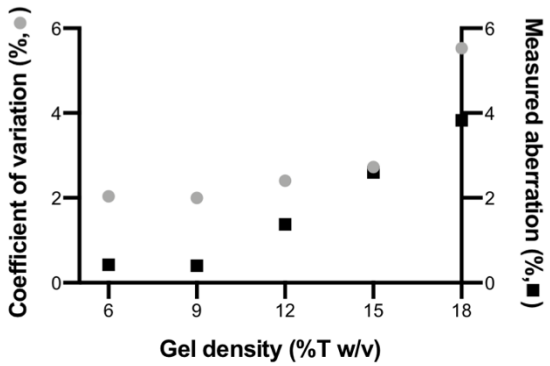

Figure S9. Comparison of the coefficient of variation between technical replicates and measured aberration ($\delta_{SIR,}$ the deviation of the SIR from 1.0).

Figure S10. Preliminary microcassette partitioning experiments using photoactivated gels.

We first tested all four possible microscale PA gel conditions (± BPMAC, ± UV-exposure) with both Ab* and Fab* using a microarray gasket (ArrayIt, AHC1X16), which allows for multiple replicates and solutes to be tested on a single gel. Microscale PA gels were fabricated on glass slides and subject to one hour of solute loading. The solutes were unloaded from the gels in a bath of TBST for one hour, with a buffer exchange after 30 minutes. The gels were then dried and imaged using a microarray scanner. The results are shown in Figure S10 below. Due to differences in degrees of labeling, the absolute fluorescence intensities measured from Ab* and Fab* cannot be cross-compared. Photoactivated BPMAC-containing gels retain considerably more Fab* and Ab* (almost an order of magnitude more) after incubation and subsequent unloading compared to gels lacking BPMAC in the presence or absence of UV exposure or gels containing BPMAC without UV exposure. Therefore, to reduce experimental complexity, *K* and retained immunoprobe fluorescence after washout were measured for the two extreme conditions: vehicle control gels and BPMAC-containing gels exposed to UV.

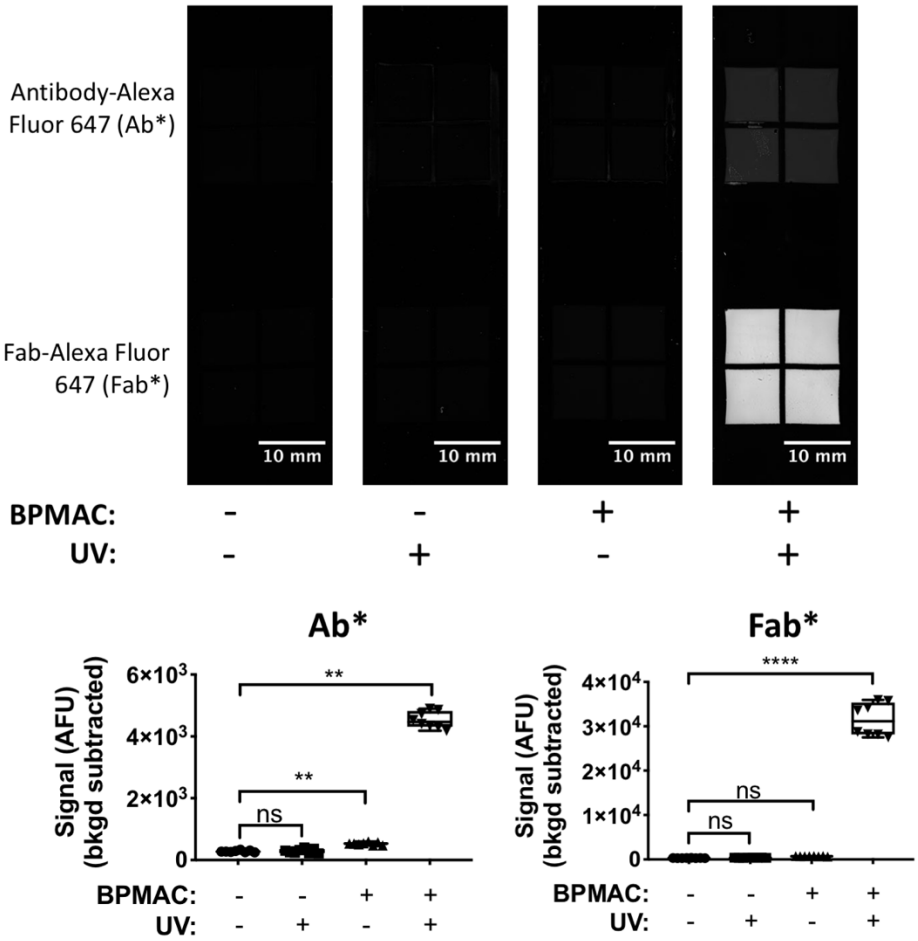

Figure S10. Representative micrographs demonstrating higher intensity of fluorescently labeled probes in BPMAC+ gels after exposure to UV (top) and quantitation of fluorescence intensity (bottom). **p < 0.05, ****p < 0.0001, ns = non-significant, N = 8 replicates, one-way ANOVA with Dunnett's multiple comparison test.

Figure S11. Retention of Ab* and Fab* after unloading from gel.

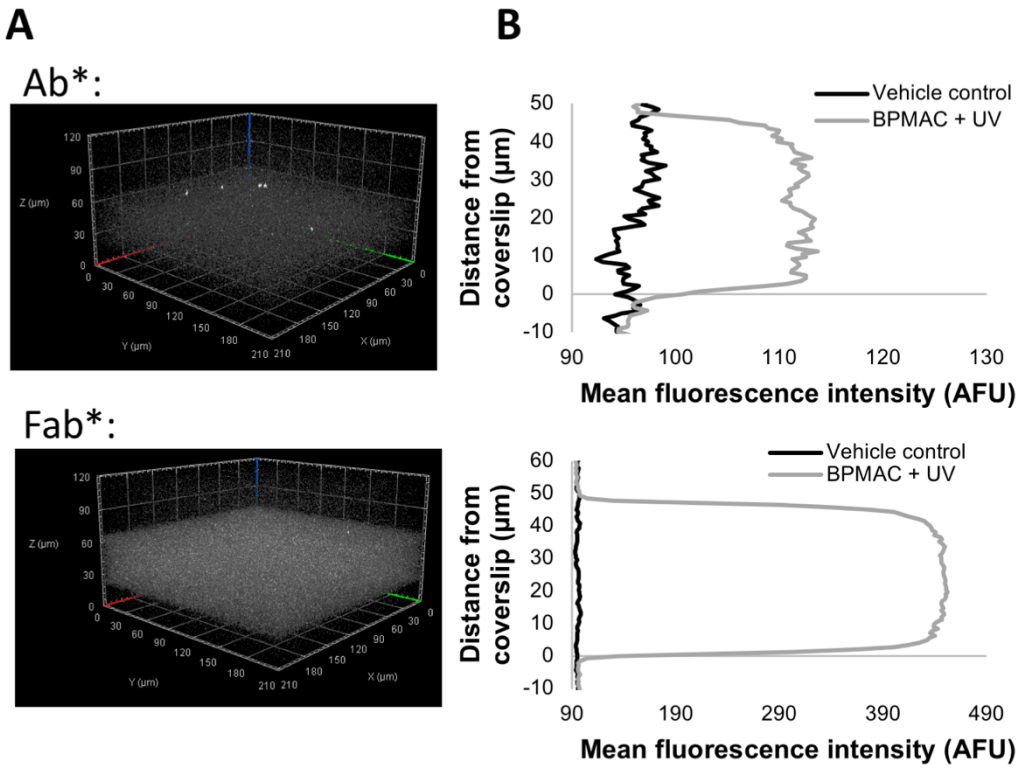

Figure S11. A) Representative micrographs of photoactivated BPMAC-containing gels (BPMAC + UV) after unloading of immunoprobe. B) Representative intensity profiles of vehicle control and BPMAC + UV PA gels comparing the retained fluorescence after unloading of immunoprobe. Note that a $1 \times 1 \times 1$ median 3D filter was applied prior to generation of the intensity profiles to reduce pixel noise.

Figure S12. Impact of median filter on quantitation.

The median filter applied for image analysis lowers the average mean intensity in-gel after unloading much more than after loading: the average mean intensity in-gel after unloading is lowered by ~55% and ~35% compared to 3.2% and 1.7% after loading for Ab* and Fab*, respectively. Therefore, the fraction of retained fluorescence in-gel is an underestimate.

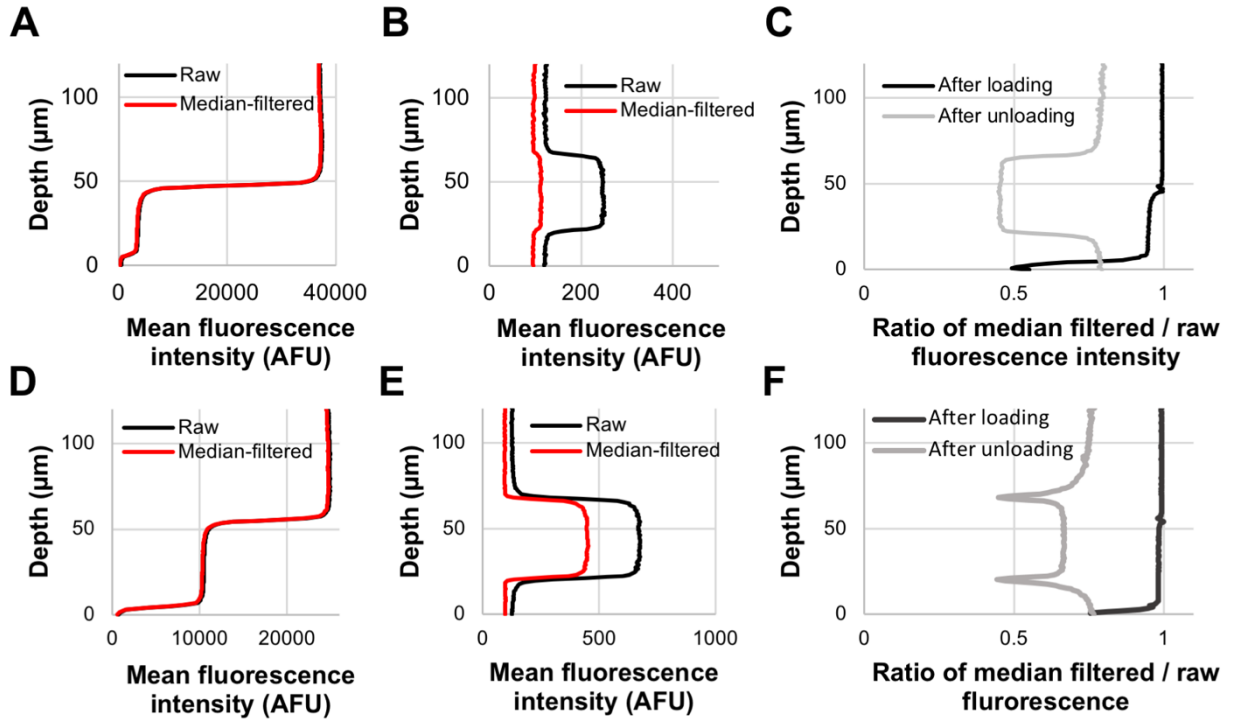

Figure S12. Differential impact of 1 × 1 × 1 median 3D filter on in-gel fluorescence intensity profiles. (A) Comparison of raw and median-filtered average fluorescence intensities with depth for gel image after loading of Ab*. (B) Comparison of raw and median-filtered average fluorescence intensities for gel image after unloading of Ab*. (C) Measured ratios of median-filtered to raw average fluorescence intensities before and after unloading of Ab*. (D-F) Same as A-C, except with Fab* as solute.

Figure S13. Two-layer gel setup and representative micrograph.

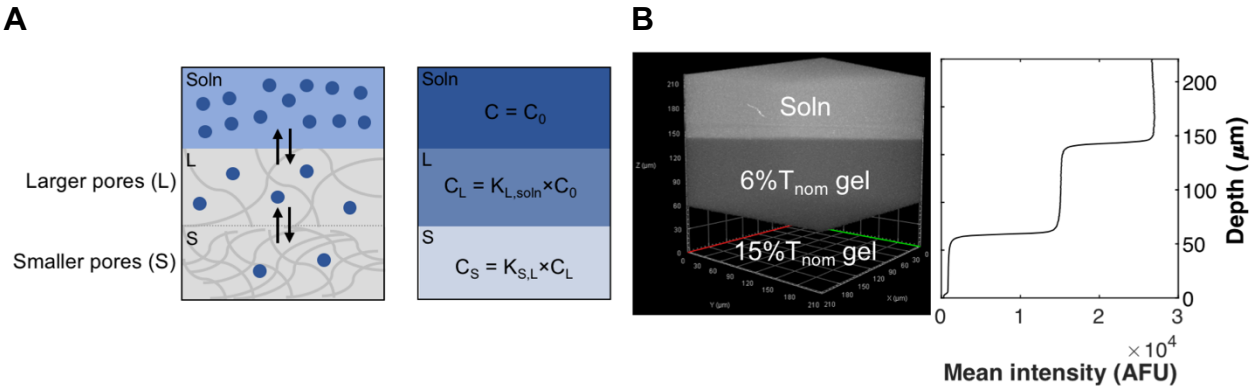

Figure S13. A) Schematic exhibiting how solute partitioning can vary axially in multi-layered gels, highlighting the importance of 3D spatial resolution. The subscripts of *K* indicate the source of the concentrations with which *K* is calculated for the equation. B) Representative fluorescence micrograph and corresponding intensity profile of two-layer gel system which is comprised of two gel layers seated on a chambered coverslip. A solution of TI* is applied to the top of the sandwich structure for the *K* measurements.

Figure S14. Impact of different gel layer configurations on *K* in two-layer composite PA gels.

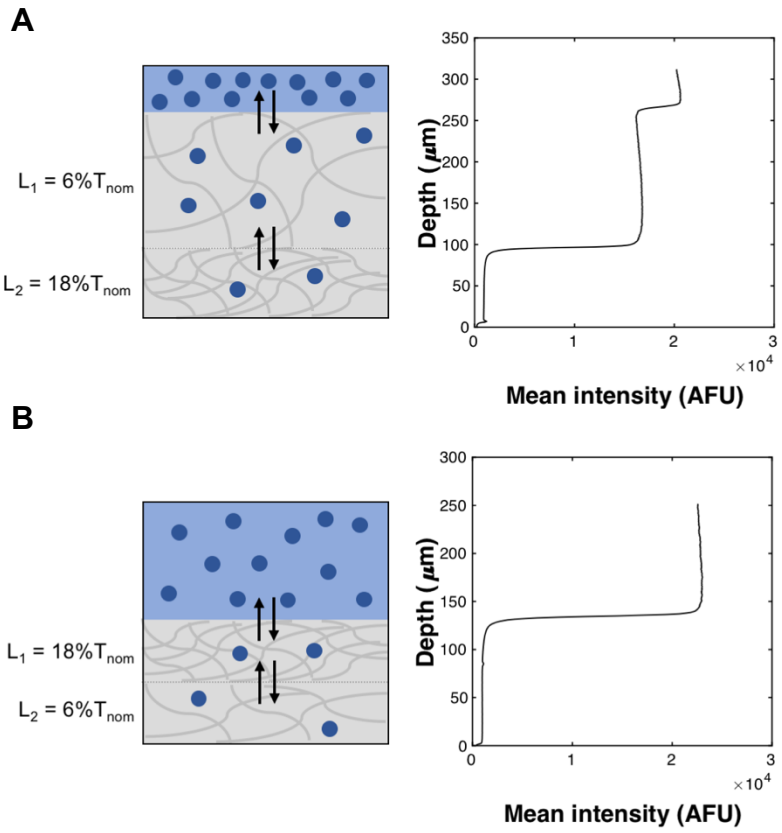

Figure S14. Schematics and representative fluorescence intensity profiles of two-layer gel systems (6%T_{nom} and 18%T_{nom}) with different gel layer configurations in equilibrium with TI*. A) Two-layer gel configuration with larger pore size 6%T_{nom} gel fabricated on top of a smaller pore size 18%T_{nom} gel. Note the distinct two different gel layers detectable using AC-LSCM. B) Two-layer gel configuration with smaller pore size 18%T_{nom} gel fabricated on top of a larger pore size 6%T_{nom} gel. Note the single homogeneous gel layer detectable using AC-LSCM. In this case, the lengths L_1 and L_2 are estimates.

Note S1. Calculation of diffusion times

Length-scale of interest is the height of the gel, z ≈ 40 μm for single layer gels, z ≈ 110 μm for two-layer gels.

Equilibration time τ for 2D diffusion: $\tau = \frac{z^2}{2D_{gel}}$
Incubating for 3τ results in > 99% diffusion to equilibrium

Hindered diffusion in PA gel[8]: $D_{gel} = D_{H_2O} \times \exp\left(-3.03{R_h}^{0.59} \times \%T^{0.94}\right)$

D_{H_2O} can be estimated from the Stokes-Einstein equation: $D_{H_20} = \frac{k_B T}{6\pi\eta_{H_20}R_h}$

<u>For TI*:</u>
R_h ≈ 24.5 Å
D_{H_2O} ≈ 100 μm²/s
Therefore, D_{gel} in an 18%T w/v PA gel (highest density gel tested) ≈ 1.85 μm²/s, and **3τ for a 40 μm gel ≈ 22 minutes.**

τ for the multilayer gels can be over-estimated by assuming a 15%T w/v PA gel that is ~110 μm tall. **3τ for a 110 μm 15%T w/v PA gel ≈ 90 minutes.**

<u>For immunoprobes:</u>
In this study, the solute that will take the longest to reach equilibrium is Ab*:
R_h ≈ 61 Å
D_{H_2O} ≈ 40 μm²/s
Therefore, D_{gel} in a 6%T w/v PA gel ≈ 3.5 μm²/s, and **3τ for a 40 μm tall PA gel ≈ 11 minutes.**

Note S2. Adjusted Ogston model

Lazzara, Blankschtein, and Deen[9] conducted an excluded volume analysis for steric interactions between multiple solutes:

$K_{TI^*} = \exp[-\phi\alpha_{TI^*,PA}(s,f) + \alpha_{TI^*,TI^*}(s,s)(1-K_{TI^*})\chi_{TI^*} + \alpha_{TI^*,BSA}(s,s)(1-K_{BSA})\chi_{BSA}]$

ϕ = polymer volume fraction
α = dimensionless interaction term
χ = solute volume fraction in bulk solution
K = partition coefficient
s = sphere, f = fiber

For this analysis, we model both TI* and BSA as spheres.
For our system, the first part of the equation reduces to Ogston's ideal size exclusion model:

$$-\phi\alpha_{TI^*,PA}(s,f) = -\phi(1 + \frac{R_{h,TI^*}}{a_f})^2$$

Since we are working with a dilute solution of TI*, the interaction term between TI* molecules goes to 0:

$$\alpha_{TI^*,TI^*}(s,s) = 0.$$

Thus, the second part of the equation goes to 0.

Finally, since the concentration of BSA in the bulk solution is quite high, we cannot ignore the third part of the equation. However, we can substitute published values for each of the terms. From Lazzara and Deen:[5]

$$\alpha_{TI^*,BSA}(s,s) = (1 + \frac{R_{h,TI^*}}{R_{h,BSA}})^3 \text{ where } R_{h,BSA} = 36 \text{ Å}$$

χ_{BSA} is related to the mass concentration of BSA (ρ_{BSA}) and the specific volume of BSA[10,11] (υ_{BSA}) by following relationship:

$$\chi_{BSA} = \rho_{BSA} \times \upsilon_{BSA} = 20\frac{g}{L} \times 7.33 \times 10^{-4}\frac{L}{g} = 0.01466$$

Tong and Anderson[12] measured the partition coefficient of BSA over varying PA volume fractions. They found that the trend of K followed Ogston's ideal size exclusion model following the best fit of:

$$K_{BSA} = \exp[-\phi\left(1 + \frac{R_{h,BSA}}{a_f}\right)^2] = \exp[-\phi\left(1 + \frac{36\text{ Å}}{5.9\text{ Å}}\right)^2].$$

Finally, the adjusted Ogston size-exclusion model for TI* becomes:

$$K_{TI^*} = \exp[-\phi\left(1 + \frac{R_{h,TI^*}}{a_f}\right)^2 + \left(1 + \frac{R_{h,TI^*}}{R_{h,BSA}}\right)^3\left(1 - \left[\exp[-\phi\left(1 + \frac{36\text{ Å}}{5.9\text{ Å}}\right)^2]\right]\right) \times 0.01466]$$

Note S3. Damköhler number analysis

To consider whether the uniformity of partitioning (used as a proxy for pore size) observed in the two-layer system contradicts the hypothesis that acrylamide diffusion causes the smaller pore sizes observed in both systems, we recall that the spatial uniformity of pore size in the bottom gel depends on whether the system is transport- or reaction-limited. This can be determined by evaluating the Damköhler number (Da) of the system, which compares the transport equilibrium time ($\tau_{transport}$) to the reaction equilibrium time ($\tau_{reaction}$): Da = $\frac{\tau_{transport}}{\tau_{reaction}}$. Chemical polymerization of acrylamide using low %C has been shown to near completion after 12-15 minutes,[13] which suggests $\tau_{treaction}$ on the order of minutes, while the small size and fast diffusivity of acrylamide lead to an estimated $\tau_{transport} \sim 2$ seconds in solution (~9 seconds in a 40 μm 15%T gel).[14] These timescales produce Da << 1, indicating a reaction-limited system. We would therefore anticipate a uniform distribution of the smaller pore size throughout the 15%T_{nom} gel, corroborating our observation (**Figure S13).**

Note S4. Method for quantifying and correcting aberration-induced depth-dependence of in-gel fluorescence

The empirical relationship between in-gel fluorescence signal and imaging depth can be established by fabricating a gel 'wedge' having a top surface with a constant incline from the coverslip to the maximum gel thickness. The gel wedge would be incubated with the fluorescent solute. The variable thickness of the gel would quantify the impact of depth-dependent aberrations on measured fluorescence (δ_{SIR}), for all z-positions in the gel. The concentration distribution of the solute – throughout the thickness of the gel – then would be determined by correcting the measured fluorescence signal by the known amount of aberration at each height. To ensure that the entire light path is contained within the gel (to avoid additional refractive errors during imaging), the angle of the gel (θ_{gel}) must be greater than the angle of the numerical aperture (NA) of the light path (Figure S15 below). Given that NA = n*sin(θ_{NA}) where θ_{NA} is the half-angle of light emerging from the objective, for the 1.1 NA objective used in this study, the angle of the gel must be greater than arcsin(NA/n) = arcsin(1.1/1.33) = 56°.

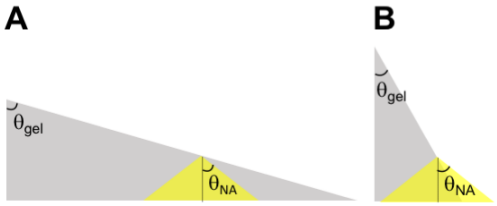

Figure S15. Schematic illustrating how the angle of the gel (θ_{gel}) must be greater than the angle of the numerical aperture of the objective (θ_{NA}) to avoid refractive errors when imaging gels with constantly increasing thickness. A) $\theta_{gel} > \theta_{NA}$. B) $\theta_{gel} < \theta_{NA}$.

References:

(1) Keller, H. E. In *Handbook of Biological Confocal Microscopy*; Pawley, J. B., Ed.; Springer, 2006; pp 145–161.
(2) Schwertner, M.; M.J., B.; Wilson, T. *J. Microsc.* **2005**, *217*, 184–187.
(3) Michielsen, S. *J. Appl. Polym. Sci.* **2001**, *81*, 1662–1669.
(4) Hell, S.; Reiner, G.; Cremer, C.; Stelzer, E. K. H. *J. Microsc.* **1993**, *169*, 391–405.
(5) Lazzara, M. J.; Deen, W. M. *J. Colloid Interface Sci.* **2004**, *272*, 288–297.
(6) Buehler, K. L.; Anderson, J. L. *Ind. Eng. Chem. Res.* **2002**, *41*, 464–472.
(7) Varshosaz, J.; Falamarzian, M. *Eur. J. Pharm. Biopharm.* **2001**, *51*, 235–240.
(8) Park, H.; Johnson, C. S.; Gabriel, D. A. *Macromolecules* **1990**, *23*, 1548–1553.
(9) Lazzara, M. J.; Blankschtein, D.; Deen, W. M. *J. Colloid Interface Sci.* **2000**, *226*, 112–122.
(10) Peters, T. In *The Plasma Proteins*; Elsevier, 1975; pp 133–181.
(11) Ratner, B. D.; Hoffman, A. S.; Schoen, F. J.; Lemons, J. E. 2004.
(12) Tong, J.; Anderson, J. L. *Biophys. J.* **1996**, *701*, 1505–1513.
(13) Gelfi, C.; Righetti, P. G. *Electrophoresis* **1981**, *2*, 213–219.
(14) Fuxman, A. M.; Mcauley, K. B.; Schreiner, L. J. *Chem. Eng. Sci.* **2005**, *60*, 1277–1293.